Journal of Magnetic Resonance **141,** 7–17 (1999)
Article ID jmre.1999.1871, available online at http://www.idealibrary.com on IDEAL®

Maps of Self-Diffusion Coefficients by Radiofrequency Field Gradient NMR Microscopy

M. Valtier, F. Humbert,[1] and D. Canet

Laboratoire de Méthodologie RMN (UPRESA CNRS 7042, FR CNRS 1742 INCM), Université H. Poincaré, Nancy I, B.P. 239, 54506 Vandoeuvre-lès-Nancy Cedex, France

Received December 7, 1998; revised June 16, 1999

The methods of measurement of spatially resolved diffusion coefficients using radiofrequency field gradient (E. Mischler *et al., J. Magn. Reson. B* 106, 32, 1995; R. Kimmich *et al., J. Magn. Reson. A* 112, 7, 1995) produce 1D profiles whose amplitude is not only a function of the local self-diffusion coefficient but also is modulated by cosine functions of spatial coordinates. Due to this modulation diffusion-weighted images cannot be obtained unless cumbersome data processing is used. Here, we present a new sequence which avoids this modulation and yields in a straightforward manner *true* self-diffusion coefficient maps; this is in contrast with conventional methods which use static field gradients and which are therefore altered by background gradients. The feasibility and the reliability of the method are demonstrated with phantoms; it is also applied to different systems of interest such as solvent swelled rubber, membranes, and plants.

Key Words: **NMR microscopy; diffusion map; radiofrequency field gradients.**

INTRODUCTION

Diffusion-weighted magnetic resonance imaging has proved to be a powerful tool in the biomedical field for characterizing biological tissues and, in particular, is especially well suited for early detection of cerebral ischemia (*1–4*). In addition, owing to its ability to provide spatially localized velocity and self-diffusion coefficients, this imaging technique is also of considerable interest in the nonmedical sciences including material science, food technology, fluid dynamics, and biotechnology (*5–8*). Applied at high spatial resolution this method is termed dynamic NMR microscopy (*9*). The basic principle relies on a combination of *k*-space and *q*-space imaging. Usually this is performed with static field gradients (B_0 gradients) incorporating a pulsed field gradient spin echo sequence into the conventional imaging experiment. From a series of images in which *q* is incremented (by successively stepping the gradient used for probing translational motions), velocity and self-diffusion maps can be obtained (*9, 10*). In fact, for most systems of interest such as porous media and biological systems, only *apparent* diffusion coefficient (ADC) maps can be obtained. The origins of this limitation are fourfold: (i) interaction between imaging and diffusion gradients (*11, 12*), (ii) presence of background (or internal) gradients appearing at boundaries between regions of different magnetic susceptibility (*13, 14*), (iii) restricted diffusion, and (iv) presence of different populations differing by their diffusion coefficients and relaxation times (*4*). Points (ii) and (iii) can be a very interesting source of information about the heterogeneous nature of materials under investigation (*4, 15, 16*). However, in order to accurately analyze diffusion measurements, it is mandatory to identify the two effects separately. Numerous methods (*12, 17–21*) have been proposed for partially mitigating the harmful effects of features (i) and (ii) on the ADC determination. They require very strong gradients (*22, 23*) or sophisticated experimental techniques (*16*). The efficiency of these methods strongly depends on the strength and nonuniformity of background gradients, on diffusion times, on the diffusion coefficient values, and on the size of regions possessing different magnetic susceptibility (*13*). To avoid the problems related to background gradients, an alternative of choice is to use radiofrequency (RF) field gradients (B_1 gradients). Indeed, it is known that this technique is insensitive to magnetic susceptibility differences within the object under investigation (*24*). In addition, in our previous work (*25–27*) we have shown that methodologies based on B_1 gradients also enable one to determine spatially resolved diffusion coefficients. Kimmich and co-workers (*28, 29*) have obtained similar results with the magnetization grid rotating frame imaging experiment. The method encodes translational diffusion affecting longitudinal magnetization with two B_1 gradient pulses of duration δ separated by an evolution interval Δ (first part of the sequence shown in Fig. 1). At the end of this sequence, taking into account the phase cycle, only the *z* component of nuclear magnetization is not zero and its intensity at a location *X* (if the *X* axis corresponds to the B_1

[1] To whom correspondence should be addressed. Current address: LCPE, VMR 9992, CNRS 1 Université H. Poincaré, Nancy I, 405, rue de Vandoeuvre, 54600 Villers-lès-Nancy, France.

1090-7807/99 $30.00

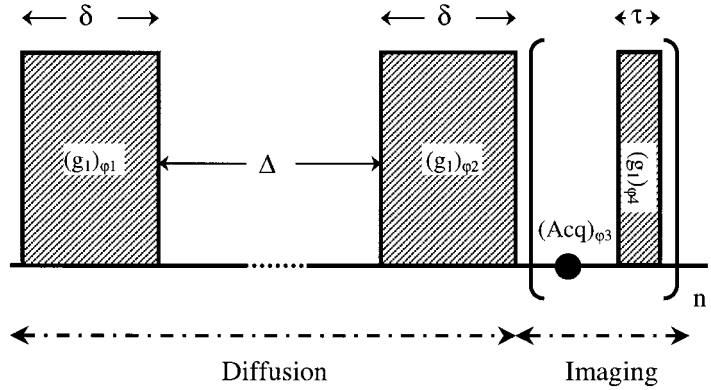

φ_1	φ_2	φ_3	φ_4
x	x	-x	x
x	-x	x	x
-x	x	-x	x
-x	-x	x	x

FIG. 1. The basic sequence and the associated phase cycling for determining spatially resolved diffusion coefficients with RF field gradients. The first part (diffusion contrast period), with two B_1 gradient pulses (hatched rectangles) of duration δ and magnitude g_1 separated by a diffusion interval Δ, produces a decrease of longitudinal magnetization according to translational diffusion. Subsequently, in the second part, the z magnetization is spatially labeled by rapid rotating frame imaging which consists of applying a train of B_1 gradient pulses each of duration τ and acquiring a data point (black dot) between two consecutive pulses. The data set constitutes a *pseudo-fid* whose Fourier transform provides a 1D profile weighted by self-diffusion coefficient and T_1 and spatially modulated.

gradient direction), in the case of unrestricted diffusion, is given by (*26*)

$$m_z = m_0(1 - \exp(-\Delta/T_1))\cos(\gamma g_1 \delta X) + m_0 \exp(-\Delta/T_1)\cos^2(\gamma g_1 \delta X)\exp(-\gamma^2 g_1^2 \delta^2 D\Delta), \quad [1]$$

where m_0, D, T_1, g_1, and γ denote the equilibrium magnetization, the diffusion coefficient, the longitudinal relaxation time, the B_1 gradient strength, and the gyromagnetic ratio, respectively. The z magnetization exists in the form of a grid which can then be visualized by rapid rotating frame imaging (second part of the sequence shown in Fig. 1). Data obtained for a series of experiments carried out with different values of Δ can be fitted according to Eq. [1] so as to provide T_1 and D as a function of spatial coordinates.

However, this method presents a drawback in the sense that it precludes us from directly obtaining a diffusion-weighted image and *a fortiori* a diffusion map because of the spatial modulation appearing in Eq. [1]. When only the global diffusion coefficient measurement is concerned, this modulation is, in principle, canceled since, for sufficiently long gradient pulses, the ensemble averages (over the sample) of $\cos(\gamma g_1 \delta X)$ and $\cos^2(\gamma g_1 \delta X)$ are 0 and $\frac{1}{2}$, respectively. However, this is not always verified experimentally (especially in the case of small and/or heterogeneous samples, of weak diffusion coefficients, and/or of very short relaxation times) and this feature is prone to affect the quality of global diffusion coefficient measurement (*30*). We have shown that, in these cases, a possible remedy is to annihilate the squared cosine modulation by combining it with a squared sine modulation; this is achieved by inserting appropriate homogeneous $\pi/2$ pulses in the basic diffusion sequence. In this paper we extend this method with the objective to directly obtain diffusion-weighted images and diffusion coefficient maps as this is currently done in conventional imaging with B_0 gradients. This method should not be considered simply as an alternative, as it offers, in addition to a remarkable experimental simplicity, the decisive advantage of being totally insensitive to background gradients.

PULSE SEQUENCE DESIGN

Basic Sequence

Figure 2 shows the pulse sequence designed to provide diffusion-weighted images by using B_1 gradients. It is composed of two subsequences A and B, each of them combining a diffusion experiment and a rotating frame imaging experiment yielding a *pseudo-fid*. To understand properly how this pulse sequence leads to spatially localized diffusion coefficients, we are going to outline the evolution of the magnetization during the sequence. Let X be the spatial direction of the RF gradient and let us consider an elementary slice at a given abscissa X corresponding to an equilibrium magnetization m_0. For the first two steps of the phase cycle given in Fig. 2, it is easy to demonstrate that just after the second gradient pulse (applied for diffusion measurement purpose) the magnetization components are, for subsequence A,

$$m_x = m_0 E_2 \sin\theta \sin\psi$$

$$m_y = m_0 E_2 \sin\theta \cos\theta' \cos\psi + m_0(1 - E_1)\sin\theta \pm m_0 E_1 \cos\theta \sin\theta'$$

$$m_z = -m_0 E_2 \sin\theta \sin\theta' \cos\psi + m_0(1 - E_1)\cos\theta \pm m_0 E_1 \cos\theta \cos\theta', \quad [2]$$

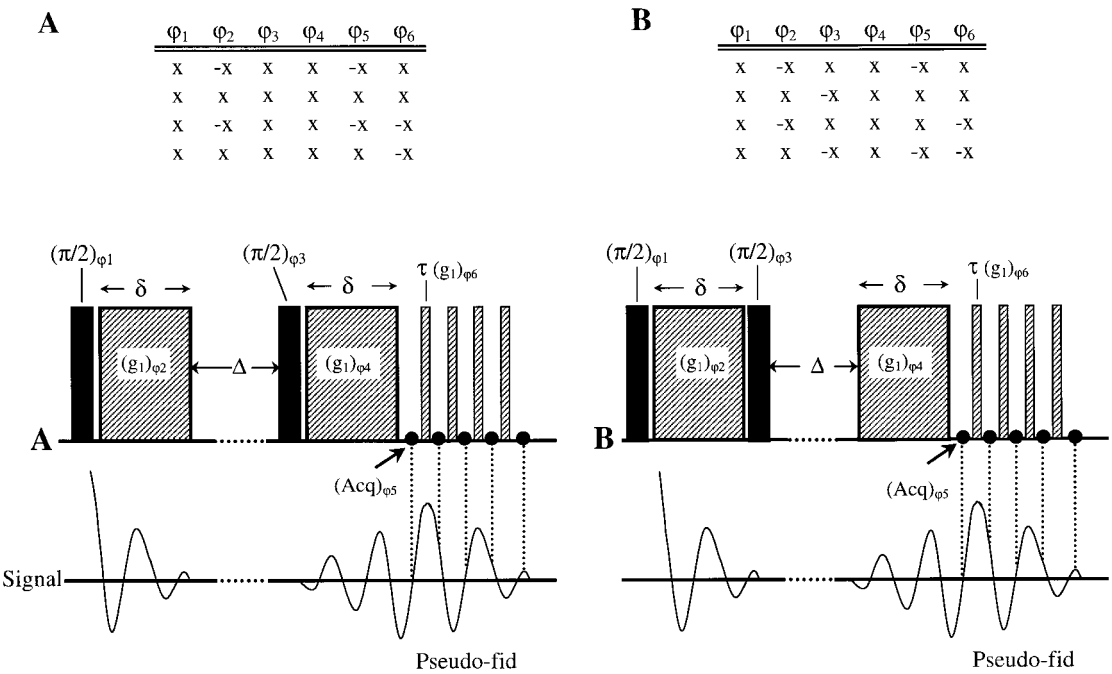

FIG. 2. The basic sequence composed of the two subsequences A and B and their associated phase cyclings for providing diffusion-weighted images with RF field gradients. The homogeneous $\pi/2$ pulses (black rectangles) inserted in the diffusion contrast period enable one to remove the spatial modulation inherent to the sequence in Fig. 1 and to retain only the signal attenuation due to diffusion. The various symbols have the same meaning as in Fig. 1.

and for subsequence B,

$$m_x = m_0 E_2 \cos\theta \sin\psi$$

$$m_y = -m_0 E_2 \cos\theta \sin\theta' \cos\psi + m_0(1 - E_1)\cos\theta \mp m_0 E_1 \sin\theta \cos\theta'$$

$$m_z = -m_0 E_2 \cos\theta \cos\theta' \cos\psi - m_0(1 - E_1)\sin\theta \pm m_0 E_1 \sin\theta \sin\theta', \quad [3]$$

where ψ is the precession angle during Δ; $E_1 = \exp(-\Delta/T_1)$ and $E_2 = \exp(-\Delta/T_2^*)$ (T_2^* the effective transverse relaxation time); θ and θ' the nutation angles due to the first and second gradient pulse, respectively. Considering the phase cycling of acquisition ($\pm x$), the components of the magnetization which actually contribute to the detected signal during the imaging sequence are

$$m_x = 0$$

$$m_y = 2 m_0 E_1 \cos\theta \sin\theta'$$

$$m_z = 2 m_0 E_1 \cos\theta \cos\theta' \quad [4]$$

for subsequence A, and

$$m_x = 0$$

$$m_y = -2 m_0 E_1 \sin\theta \cos\theta'$$

$$m_z = 2 m_0 E_1 \sin\theta \sin\theta' \quad [5]$$

for subsequence B.

Summing up the contributions of both subsequences and dividing by the number of steps we obtain

$$m_x = 0$$

$$m_y = -m_0 E_1 \sin\varphi$$

$$m_z = m_0 E_1 \cos\varphi \quad \text{with } \varphi = \theta - \theta'. \quad [6]$$

Although both gradient pulses δ are identical, φ is not necessarily zero because of translational molecular motions along the B_1 gradient direction during Δ. Thus, considering a time average over Δ (denoted below by a bar), the contribution of the considered elementary slice to the lth data point (l positive integer) acquired during the imaging gradient pulse train can be written

$$s(\Delta, \delta, X, l) = \frac{m_0 E_1}{2}\left[\overline{\cos\varphi}\,\sin(\gamma g_1 X l \tau) + \overline{\sin\varphi}\,\cos(\gamma g_1 X l \tau)\right], \quad [7]$$

where τ is the length of each pulse.

In the above equation, possible precession effects which could occur during the acquisition windows have been neglected. In the case of free diffusion process, a Gaussian distribution describes adequately molecular displacements leading to $\overline{\sin\varphi} = 0$ and $\overline{\cos\varphi} = \exp(-\gamma^2 g_1^2 \delta^2 D \Delta)$. However, these relations no longer hold if we are concerned with restricted diffusion and, in such a situation, it becomes necessary to cancel the second term of Eq. [7]. This is easily achieved by inverting all the phase signs in the imaging sequence, hence the third and fourth step of the phase cycle. Thus, regardless of the diffusion process, the intensity of lth acquired point can be expressed as

$$S(\Delta, \delta, k) = \int_{\text{object}} \frac{m_0 E_1}{2}\,\overline{\cos\varphi}\,\sin(2\pi k X)\,dX, \quad [8]$$

with $k = (2\pi)^{-1}\gamma g_1 l \tau$.

Fourier transformation of the whole data set (*pseudo-fid*) yields the diffusion-weighted profile along the gradient direction, the amplitude ρ at abscissa X being directly related to the local diffusion coefficient $D(X)$ and longitudinal relaxation time $T_1(X)$ by the relation

$$\rho(X) = \frac{m_0}{2}\exp(-\Delta/T_1(X))\exp(-\gamma^2 g_1^2 \delta^2 D(X)\Delta). \quad [9]$$

It is important to note that, by contrast with Eq. [1], Eq. [9] is devoid of any spatial modulation and that, for an unrestricted diffusion process, D corresponds to the *true* local self-diffusion coefficient.

By rotating the sample and recording a profile for each new orientation, a diffusion-weighted image can be reconstructed through algorithms currently in use (*31, 32*). Subsequently, pixel-by-pixel analysis according to Eq. [10] from a series of diffusion-weighted images, performed by successively stepping the gradient pulse duration δ, yields a diffusion coefficient map. It is important to note that the method used to reconstruct diffusion-weighted images precludes the study of diffusion anisotropy. This feature could only be examined by 1D imaging.

Alternative Sequence with Acquisition of a Pseudo-echo

It can be realized that the experiment described in the previous section amounts to sampling the right part of the rotary echo induced by the second δ gradient pulse. As seen above, the echo amplitude depends on diffusion process during Δ while spatial information is contained in the pseudo-fid. Nevertheless, following the example of imaging experiments with B_0 gradients, it might be interesting to be able to sample the whole echo. Indeed, it is well known that the full echo sampling confers some advantages (*33*). In particular, there is no dispersion spectrum. Consequently, it is possible to directly obtain the image by taking the modulus of the real and imaginary parts of the resulting transforms before calculating the filtered back-projections. This avoids difficulties associated with phase correction. In addition, the full echo sampling can be very helpful when the position of the echo maximum shifts from one experiment to the other. This occurs when the two δ gradient pulses are not strictly equivalent in terms of gradient amplitude either because of radiofrequency power amplifier instabilities (or deficiency) or because the δ/Δ ratio is larger than the duty cycle (*30*). The simplest method to acquire the full echo is to replace the second δ gradient pulse by a pulse train leading to the sequence depicted in Fig. 3, which involves the acquisition of a *pseudo-echo* (this terminology is used in reference to the *pseudo-fid* in the rapid rotating frame imaging). For simplicity we shall assume for the moment that $\tau_r = 0$ (τ_r being duration of a prerefocusing pulse as defined below) and that δ is sufficiently long to induce a complete defocusing of the magnetization. If we denote ϵ' the flip angle due to one pulse in the pulse train then the total flip angle α' for m pulses can be written

$$\alpha' = m\epsilon' \quad \text{with } 2n \geq m \geq 1$$

or

$$\alpha' = \theta' + l\epsilon' \quad \text{with } n \geq l \geq -n,$$

where the angle θ' has the same meaning as in Eqs. [4] and [5]. Consequently, at mth data, following Eqs. [5] and [6] and taking account the two phase cycle steps, the intensity arising from the considered elementary slice is

$$s(\Delta, \delta, X, l) = \frac{m_0 E_1}{2}\left[\overline{\cos\varphi}\,\sin(\gamma g_1 X l \tau) + \overline{\sin\varphi}\,\cos(\gamma g_1 X l \tau)\right]. \quad [10]$$

This latter expression is similar to Eq. [7] except that now the full echo is sampled. Thus, provided that restricted diffusion is negligible ($\overline{\sin\varphi} \approx 0$), this sequence allows one to reconstruct diffusion coefficient maps too.

So far, diffusion during the acquisition windows of the pulse train has not been considered although the whole

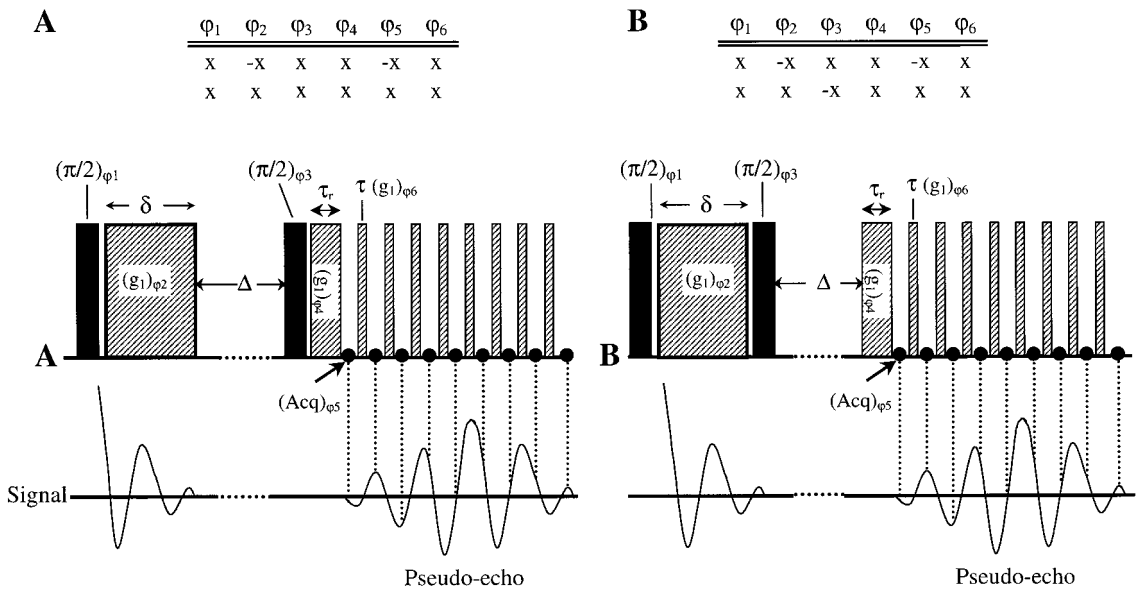

FIG. 3. An alternative to the sequence of Fig. 2, based exactly on the same principle but where the *whole* rotary echo is sampled. The acquired data set constitutes a *pseudo-echo.* The gradient pulse of duration τ_r is a prerefocusing pulse which is required so that the echo is always sampled in the same way regardless of the δ value: $\delta = \tau_r + (n/2)\tau$ where n is the total number of points of pseudo-echo. This sequence may lead to improper results in the case of restricted diffusion.

duration to acquire the n points may be nonnegligible with respect to Δ. Indeed, in practice the duration of one acquisition window is between 30 and 50 μs and the number of points of pseudo-echo is usually 256. In fact, this additional diffusion does not affect the resulting diffusion map provided that the number of points used for sampling the echo remains constant throughout the whole experiment. In these conditions, the diffusion during the acquisition windows is always encoded in the same way since the pulse length in the pulse train is constant. This implies, however, that the imaging pulse train must always be located in the same manner with respect to the echo position. This is achieved by inserting, before the pulse train, a prerefocusing gradient pulse of duration τ_r such that $\delta = \tau_r + (n/2)\tau$.

In the case of restricted diffusion it is necessary to cancel the term $\overline{\sin \varphi}$ which may be nonzero as diffusion in opposite directions does not involve the same probability. Unfortunately, the phase cycle used for this purpose in the basic sequence cannot be directly applied here because it amounts to sampling alternatively the positive and negative k values of the echo. However, it turns out that it is possible to achieve a similar result by delaying the echo formation by means of an

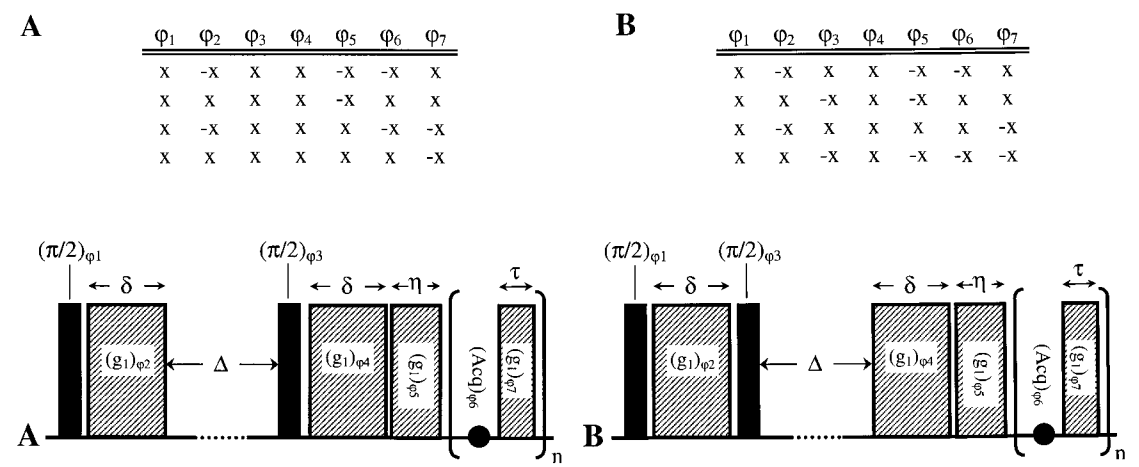

FIG. 4. The more general sequence and its associated phase cycling for providing diffusion-weighted images with RF field gradients. Thanks to the gradient pulse of duration η which delays the echo formation, it combines the advantages of the full echo sampling (as in the sequence of Fig. 3) and the possibility of determining accurately the localized diffusion coefficients by means of the basic phase cycling (sequence of Fig. 2).

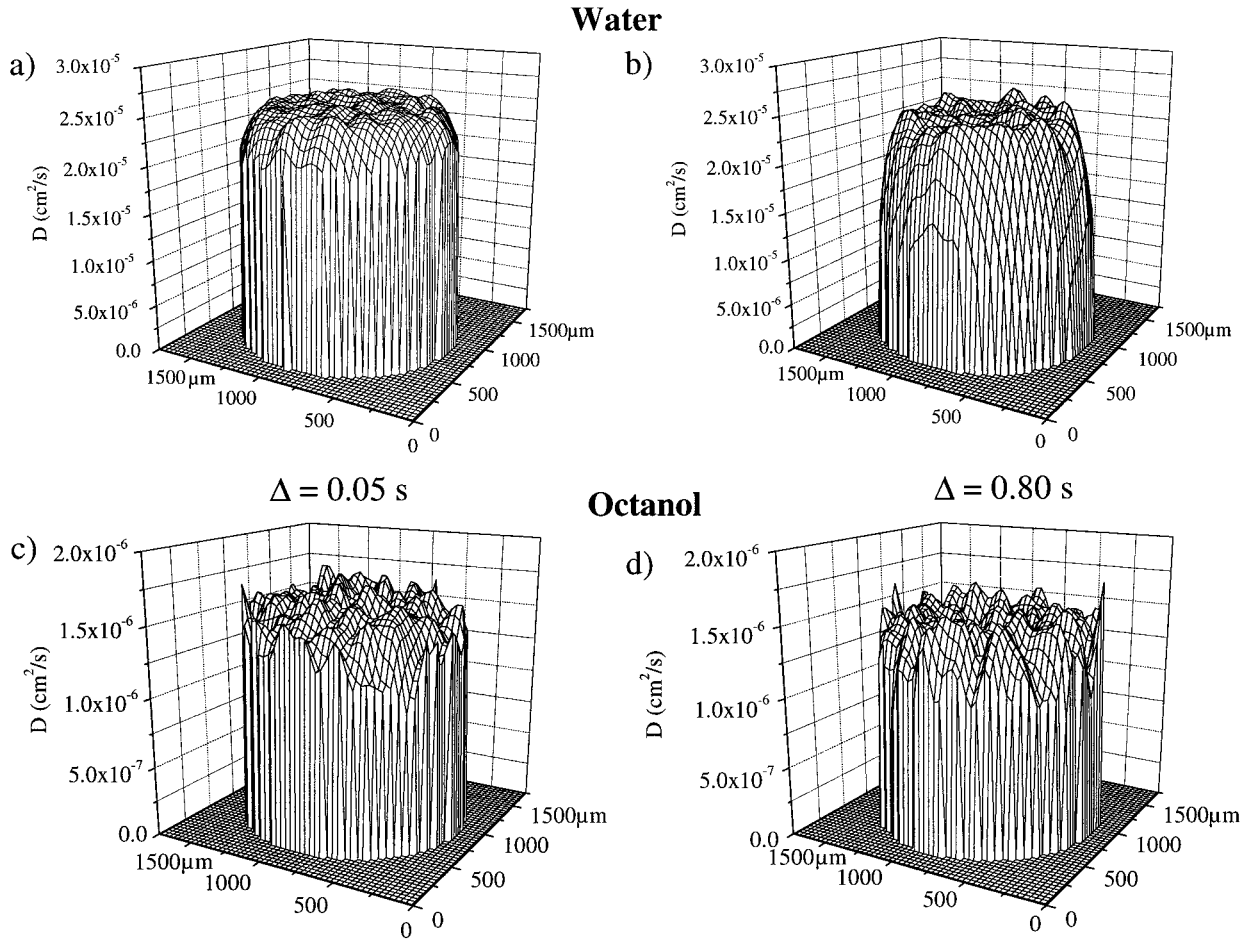

FIG. 5. The self-diffusion coefficient maps of two capillaries of 1.3-mm id filled, respectively, with water (a, b) and with octanol (c, d). The diffusion times Δ were, respectively, 0.05 s (a, c) and 0.8 s (b, d). Gradient strength g_1: 50 G cm^{-1}, angle increment used in the 2D imaging process: 6°, 64 scans for each angle increment, slice thickness: 2 mm, spatial resolution: 11 μm. These maps result from a series of five diffusion-weighted images obtained by using the sequence shown in Fig. 2 with (a) δ =10, 350, 450, 600, 750 μs; (b) δ = 10, 75, 100, 140, 175 μs; (c) δ = 10, 450, 750, 1400, 1750 μs; (d) δ = 10, 100, 250, 400, 500 μs.

additional defocusing pulse. The whole sequence is schematized in Fig. 4. Except for the defocusing pulse, the phase cycling is identical to the one given in Fig. 2. Thus this latter sequence combines the advantages of the full echo sampling and the possibility to determine properly the localized diffusion coefficients regardless of the diffusion process (free or restricted).

EXPERIMENTAL RESULTS

Materials and Methods

All experiments reported below were obtained with a Bruker Biospec BNT 100 operating at 100 MHz or with a homebuilt spectrometer equipped with a 2.1-T electromagnet (proton resonance frequency, 90 MHz). For both spectrometers the RF probe includes a flat concentric two-turn coil generating the B_1 gradient and a Helmholtz coil for collecting the NMR signal and producing homogeneous pulses (*34*). The gradient strength was 50 G cm^{-1}, the RF field amplitude varying from 17 to 32 G across samples with diameters of 3 mm. The 90° homogeneous pulse length was about 2.75 μs. The sample temperature was regulated at 25°C.

Diffusion-weighted images were obtained using the following parameters: field of view = 1.5 × 1.5 mm using 200 × 200 pixels, angle increment (for going to a new orientation) = 6 or 3.6°, 64 scans for each orientation, train pulse duration = 2.5 μs, acquisition window length = 50 μs, number of data points for defining an echo = 128 or 256. Each diffusion map was then calculated using a pixel-by-pixel two-parameters least-squares exponential fit applied to a series of two to six diffusion-weighted images.

In order to test the efficiency of the above-proposed sequences and to illustrate the wide range of applications, four systems, quite different in nature, have been investigated: (1) phantoms consisting of capillaries with diameters of 1.3 to 0.275 mm and filled with water or octanol; (2) rubber pieces

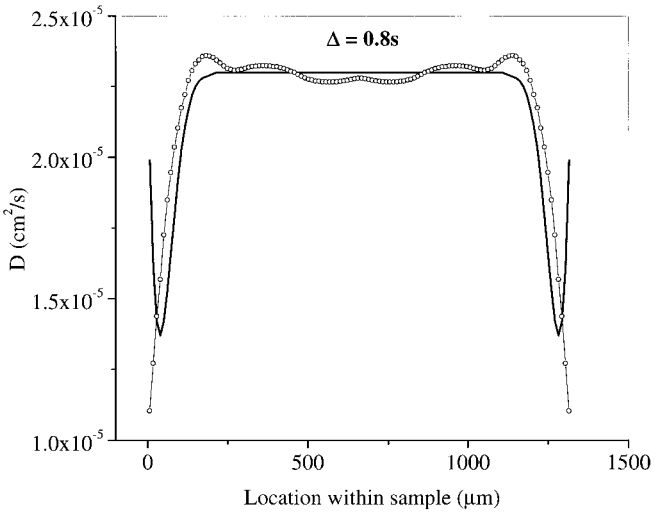

FIG. 6. Comparison of experimental average profile (open circles) extracted from the water diffusion coefficient map shown in Fig. 5b with the theoretical profile (line) obtained from Eq. [11].

with different cross-linked densities swelled by toluene; (3) a Millipore membrane immersed in water; and (4) a section of geranium petiole.

TABLE 1

Water Experimental and Theoretical Self-Diffusion Coefficients, D (in 10^5 cm^2 s^{-1}), Resulting from a Spatial Average over Only the Sample Core or over the Whole Sample

Diffusion time Δ (ms)	Experiment	D (averaged over the sample core)	D (averaged over the whole sample)	D theoretical (averaged over the whole sample)
		1.3 mm id capillary		
50	(a)	2.34	2.28	2.27
	(b)	2.33	2.26	
	(b)[a]	2.35	2.28	
300	(a)	2.36	2.26	2.23
	(b)	2.34	2.22	
800	(a)	2.33	2.15	2.18
		0.270 mm id capillary		
10	(b)	2.32	2.23	2.24
50	(a)	2.39	2.15	2.16
	(b)	2.36	2.17	
300	(a)	2.29	1.81	1.95

Note. The average is deduced from localized diffusion coefficients extracted from diffusion maps obtained by using (a) the sequence in Fig. 2 (with pseudo-fid acquisition) or (b) the sequence in Fig. 4 (with pseudo-echo acquisition). The theoretical values were calculated from Eq. [11] and by taking 2.3 10^{-5} cm^2 s^{-1} as water diffusion coefficient at 25°C. Experimental uncertainty = 5%.

[a] Acquisition window of 100 μs duration instead of 50 μs used for all other experiments.

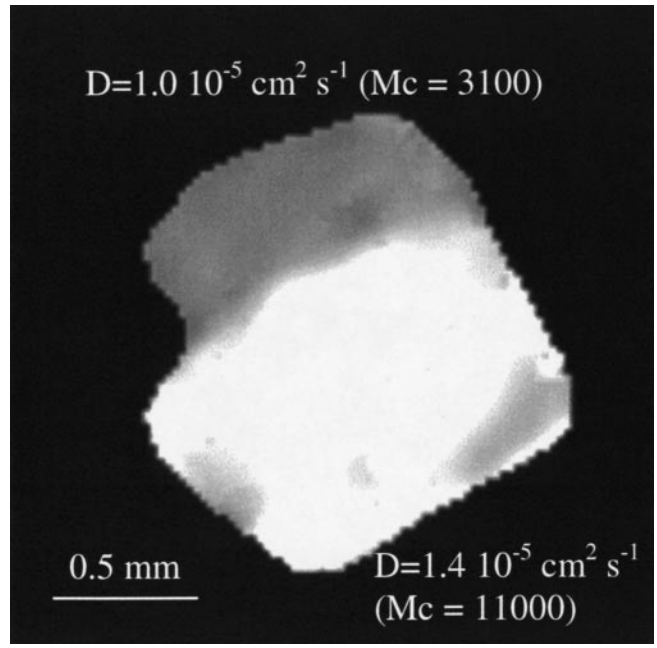

FIG. 7. The self-diffusion coefficient map obtained at 25°C with the sequence in Fig. 2 for toluene swelling two polysulfidic cross-linked natural rubber samples placed side by side. The molecular masses (Mc) of intercross-link chains are, respectively, 11,000 and 3100. The map results from a series of eight diffusion-weighted images obtained by incrementing δ from 200 up to 2000 μs. Slice thickness 2 mm; g_1 = 50 G cm^{-1}; Δ = 100 ms.

Diffusion Map of Water and Octanol Capillaries

Figure 5 shows the self-diffusion coefficient maps obtained, respectively, for water and octanol capillaries at two different diffusion times Δ by using the sequence of Fig. 2. We note that the self-diffusion coefficients calculated through the samples are in excellent agreement with the expected values at 25°C (D_{water} = 2.3 10^{-5} cm^2/s and D_{octanol} = 1.4 10^{-6} cm^2/s) except on the water capillary periphery where the diffusion coefficient value drops continuously as the distance from the wall decreases, this effect being more pronounced as the diffusion time Δ increases. On the other hand, the octanol capillary does not exhibit such a so-marked behavior. These well-characterized features suggest that these anomalies should be merely the consequence of restricted diffusion occurring close to the capillary wall. Two additional results confirm this interpretation. First, the toluene self-diffusion coefficient maps (D_{toluene} = 2.27 10^{-5} cm^2 s^{-1} at 25°C) obtained in the same conditions as those described previously are quite similar to those of water. Consequently, this result excludes any influence of the dielectric constant ϵ (ϵ_{water} = 78.5, $\epsilon_{\text{toluene}}$ = 2.4). Second, and this is a key point, spatial variations of the measured apparent self-diffusion coefficient can be described in a satisfactory way by using a relatively simple one-dimensional model which is adapted to the situation of molecules diffusing close to a reflective wall perpendicular to the gradient direction. This model, described in detail elsewhere, assumes that only one

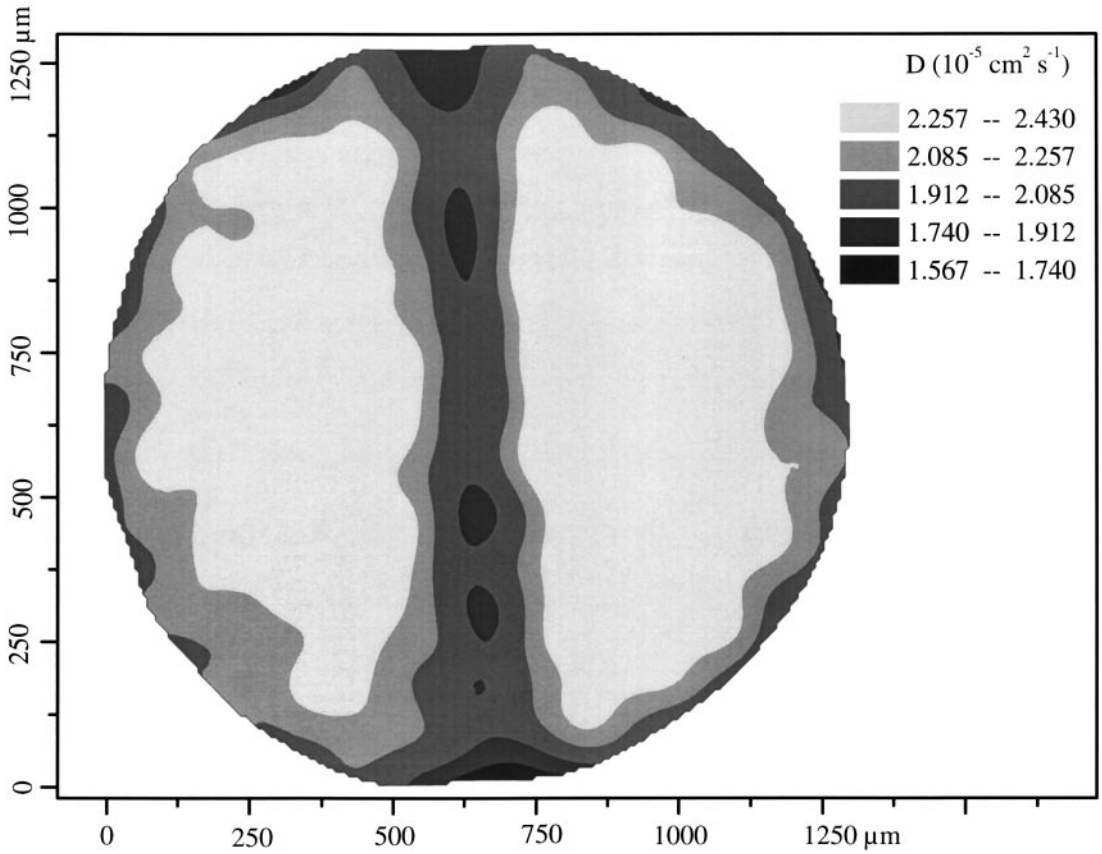

FIG. 8. The self-diffusion coefficient map obtained using the sequence in Fig. 4 for water (with a small amount of copper sulfate) outside and inside a Millipore HVLP membrane of 120-μm thickness and with a pore size of 0.45 μm. The membrane of 2-mm height was perfectly fitted into a Teflon cylindrical holder of 1.3-mm inner diameter. The map results from a series of four diffusion weighted images with, respectively, $\delta = 290$, 500, 650, and 750 μs. $g_1 = 50$ G cm^{-1}; $\Delta = 50$ ms.

reflection can occur during the diffusion interval Δ. Considering the short diffusion intervals used here as well as the size of the investigated objects, this latter assumption should not be unreasonable since the probability of two or more reflections becomes significant only over an extremely short distance from the wall, presumably inferior to the imaging resolution of 11 μm. Thus, according to this model, the diffusion coefficient localized at the abscissa X is given by

$$D_{\text{app}}(X) = D + \frac{X^2}{\Delta}\left[1 - \text{erf}\left(\frac{X}{2\sqrt{D\Delta}}\right)\right] - 2X\sqrt{\frac{D}{\pi\Delta}}\exp\left(-\frac{X^2}{4D\Delta}\right), \qquad [11]$$

where erf is the error function whose value can be found in tables of the normal probability function. This expression is identical to the one derived by Song *et al.* (*35*). As shown in Fig. 6, the experimental localized self-diffusion coefficients match the theoretical values derived from Eq. [11]. The slight differences may originate from the lack of perfect orthogonality of the capillary with respect to the gradient direction, from the slice thickness, or from relaxation phenomena at the wall location (*36*). This good agreement between experimental and theoretical values is also confirmed in Table 1 in which are reported, for various experimental conditions, the self-diffusion coefficients resulting from an average over the whole sample or only over the sample core. Moreover, we note that the two sampling methods detailed in the theoretical part (pseudo-fid or pseudo-echo acquisition) yield the same results.

It is somewhat surprising that, in spite of the abundant NMR literature about diffusion processes which has appeared since the seminal paper of Stejskal and Tanner in 1968 (*37*), such maps, to our knowledge, have not been reported. They are, however, essential in the sense that they lead to the visualization, in a simple way, of restricted diffusion effects. To date, only edge enhancements originating from the partially restricted diffusion at the sample boundaries have been observed in magnetic resonance imaging (*38, 39*). Recently, Song *et al.* (*35*) have characterized the effects of diffusion on MRI of a one-dimensional sample involving polarized xenon gas ($D_{\text{xenon}} = 0.0565$ cm^2 s^{-1} at 1 atm); however, no diffusion coefficient

map is presented in this study. Actually, difficulties met until now to obtain such maps originate probably from the use of B_0 gradients which are known to be very sensitive to background gradients (especially those appearing at the glass wall). By contrast, the B_1 gradient immunity to the magnetic susceptibility variations makes the present method particularly well suited to studying subtle diffusion differences occurring at interfaces.

Applications

Having demonstrated the feasibility and the reliability of the proposed method, we end up with three examples which illustrate its potentiality. The first two, in Figs. 7 and 8, concern material science. Figure 7 shows the self-diffusion coefficient map of toluene swelling two polysulfidic cross-linked natural rubber samples placed side by side. Each sample was immersed in toluene at 25°C until achievement of the fully swollen state. Subsequently, the two samples were sealed in a 4-mm-diameter NMR tube in the presence of a toluene-imbibed cotton in order to maintain constant the solvent concentration distribution while the images were acquired. We note that the map exhibits two diffusion coefficient values of 1.5 and 1.0 10^{-5} cm^2 s^{-1} corresponding precisely to the two rubber samples. These two values, related to different molecular masses of intercross-link chains (11,000 and 3100, respectively), reflect the difference of cross-linked density in the two samples probed by the solvent diffusion coefficient value, a property well known from previous studies (*40, 41*). The most interesting feature of this map is the achieved relatively high spatial resolution (ca. 10 μm) which is especially well illustrated by the sharp border between the two rubber pieces.

The second example is related to the behavior of fluids within porous materials such as membranes. Figure 8 shows the self-diffusion map of water outside and inside a Millipore HVLP membrane of 120-μm thickness and with a pore size of 0.45 μm. The membrane was perfectly fitted into a Teflon cylindrical holder of 1.3-mm inner diameter. As expected, the hindrance encountered by the water molecules inside the membrane leads to diffusion coefficient values which are significantly smaller inside the membrane than outside (about 1.9 and 2.3 10^{-5} cm^2 s^{-1}, respectively). In addition, the diffusion coefficient values drop slowly not only in the vicinity of the holder wall, as in Fig. 5, but also in the vicinity of the membrane, approximately in a layer of 30-μm thickness on either side of the membrane. It is also interesting to note that, in Fig. 8, the two restriction effects, due to the membrane and to the holder wall, respectively, add up at the ends of the membrane and reinforce the lowering of the localized diffusion coefficients, hence the widening of the isodensity surfaces.

Finally, the third example concerns plant imaging. Figure 9 shows the self-diffusion coefficient map obtained for a geranium petiole section of 1-mm thickness. Four zones clearly show up: the parenchyma in the middle of the stem ($D_{app} \approx 2.1$ 10^{-5} cm^2 s^{-1}), the cortex on the periphery ($D_{app} \approx 1.4$ 10^{-5} cm^2 s^{-1}), the fibrous sheath separating the cortex and the parenchyma ($D_{app} \approx 1.2$ 10^{-5} cm^2 s^{-1}), and the vascular bundles ($D_{app} \approx 0.8$ 10^{-5} cm^2 s^{-1}). It is known (*4, 42*) that the variation of the diffusion coefficient according to the biological tissue reflects not only the difference of nature between the diffusing molecules (bound or unbounded water, macromolecule) but also the molecule confinement rate which is directly related to the cell size. It is this latter feature which is partly at the origin of the large contrast observed in Fig. 9 between the parenchyma and the cortex. Indeed, the motion of a water molecule of which the root mean square displacement is about 10 μm during a diffusion time of 20 ms is more hindered in the cortex cells (typically of 10 to 50 μm diameter) and in the fibrous sheath cells (10 to 15 μm diameter) than in the much larger parenchyma cells (40 to 100 μm diameter). Consequently the apparent diffusion coefficient is lower in the cortex and the fibrous sheath than in the parenchyma. Moreover the decrease of these observed diffusion coefficients as Δ increase is quite characteristic of the restricted diffusion.

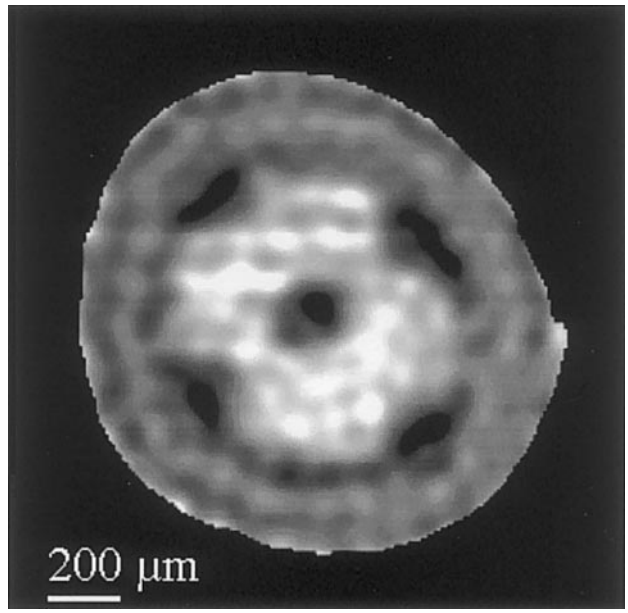

FIG. 9. The self-diffusion coefficient map obtained using the sequence in Fig. 4 for a geranium petiole section of 1-mm thickness. The map results from two diffusion-weighted images with, respectively, $\delta = 340$ and 1400 μs. Angle increment used in the 2D imaging procedure: 3.6° (see text); $g_1 = 50$ G cm^{-1}; $\Delta = 20$ ms.

CONCLUSION

We have shown here that radiofrequency field gradient NMR microscopy is able to produce self-diffusion coefficient maps of high quality. The present method represents more than a simple alternative to the conventional methods with B_0

gradients. Indeed, its quasi-immunity to background gradients and the possibility of measuring spatially the *true* diffusion coefficient make this technique particularly well suited to diffusion studies at interfaces and in heterogeneous systems such as porous media or biological tissues. In particular, it enabled us to visualize clearly and accurately, as far as diffusion coefficients are concerned, restricted diffusion in the vicinity of reflective walls. These results agree perfectly with an appropriate theoretical model. Moreover the successful application to systems of various interest such as plants, membranes, and elastomers demonstrates its reliability and its potentiality.

REFERENCES

1. B. J. Dardzinski, C. H. Sotak, M. Fisher, Y. Hasegawa, L. Li, and K. Minematsu, Apparent diffusion coefficient mapping of experimental focal cerebral ischemia using diffusion-weighted echo-planar imaging, *Magn. Reson. Med.* **30,** 318 (1993).
2. Y. Xia, T. Farquhar, N. Burton-Wurster, E. Ray, and L. W. Jelinski, Diffusion and relaxation mapping of cartilage-bone plugs and excised disks using microscopic magnetic resonance imaging, *Magn. Reson. Med.* **31,** 273 (1994).
3. Y. Yang, S. Xu, M. J. Dawson, and P. C. Lauterbur, Diffusion measurement in phantoms and tissues using SLIM mocalization, *J. Magn. Reson.* **129,** 161 (1997).
4. Y. Assaf and Y. Cohen, Non-mono-exponential attenuation of water and *N*-acetyl aspartate signals due to diffusion in brain tissue, *J. Magn. Reson.* **131,** 69 (1998).
5. W. S. Price (and references herein), "NMR Imaging, Annual Reports on NMR Spectroscopy," Vol. 35, p. 140, Academic Press, London, (1998); "Gradient NMR," Vol. 32, p. 51, Academic Press, London (1996).
6. D. M. Schmidt, J. S. George, S. I. Pentila, A. Capriham, and E. Fukushima, Diffusion imaging with hyperpolarized ^{3}He gas, *J. Magn. Reson.* **129,** 184 (1997).
7. J. Kärger, G. Seiffert, and F. Stallmach, Space and time resolved PFG NMR self-diffusion measurements in zeolites, *J. Magn. Reson. A* **102,** 327 (1993).
8. M. M. Britton and P. T. Callaghan, NMR Microscopy and the non-linear rheology of food materials, *Magn. Res. Chem.* **35,** 537 (1997).
9. P. T. Callaghan, and Y. Xia, Velocity and diffusion imaging in dynamic NMR microscopy, *J. Magn. Reson.* **91,** 326 (1991).
10. Y. Xia, K. R. Jeffrey, and P. T. Callaghan, Purpose designed probes and their application for dynamic NMR microscopy in an electromagnet, *Magn. Reson. Imaging* **10,** 411 (1992).
11. M. Neeman, J. P. Freyer, and L. O. Sillerud, Pulsed-gradient spin-echo diffusion studies in NMR imaging. Effects of the imaging gradients on the determination of diffusion coefficients, *J. Magn. Reson.* **90,** 303 (1990).
12. J. Mattiello, P. J. Basser, and D. LeBihan, Analytical expressions for the *b* matrix in NMR diffusion imaging and spectroscopy, *J. Magn. Reson. A* **108,** 131 (1994).
13. M. D. Hürlimann, Effective gradients in porous media due to susceptibility differences, *J. Magn. Reson.* **131,** 232 (1998).
14. J. D. Trudeau, W. T. Dixon, and J. Hawkins, The effect of inhomogeneous sample susceptibility on measured diffusion anisotropy using NMR imaging, *J. Magn. Reson. B* **108,** 22 (1995).
15. J. Pfeuffer, U. Flögel, W. Dreher, and D. Leibfritz, Restricted diffusion and exchange of intracellular water: Theoretical modelling and diffusion time dependence of 1H NMR measurements on perfused glial cells, *NMR Biomed.* **11,** 19 (1998).
16. M. A. Horsfield, S. A. Clark, and T. J. Norwood, Estimation of the characteristic length scales for B_0 variation using the OE-CTPG pulse sequence, *J. Magn. Reson. A* **122,** 222 (1996).
17. R. F. Karlicek, Jr., and I. J. Lowe, A modified pulsed gradient technique for measuring diffusion in the presence of large background gradients, *J. Magn. Reson.* **37,** 75 (1980).
18. X. Hong and W. T. Dixon, Measuring diffusion in inhomogeneous systems in imaging mode using antisymetric sensetizing gradients, *J. Magn. Reson.* **99,** 561 (1992).
19. L. L. Latour, L. Li, and C. H. Sotak, Improved PFG stimulated-echo method for the measurement of diffusion in inhomogeneous fields, *J. Magn. Reson. B* **101,** 72 (1993).
20. J. Lian, D. S. Williams, and I. J. Lowe, Magnetic resonance imaging of diffusion in the presence of background gradients and imaging of background gradients, *J. Magn. Reson. A* **106,** 65 (1994).
21. D. van Dusschoten, P. A. de Jager, and H. van As, Flexible PFG NMR desensitized for susceptibility artifacts, using the PFG multiple-spin-echo sequence, *J. Magn. Reson. A* **112,** 237 (1995).
22. P. Kinchesh, E. W. Randall, and K. Zick, The elimination of magnetic susceptibility distortions in the imaging of liquids in solids: The Stray Field Imaging Technique, *J. Magn. Reson.* **100,** 411 (1992).
23. C. J. Rofe, J. van Noort, P.J. Back, and P. T. Callaghan, NMR microscopy using large, pulsed magnetic field gradients, *J. Magn. Reson. B* **108,** 125 (1995).
24. R. Raulet, J. M. Escanyé, F. Humbert, and D. Canet, Quasi-immunity of B1 gradient NMR microscopy to magnetic susceptibility, *J. Magn. Reson. A* **119,** 111 (1996).
25. E. Mischler, F. Humbert, and D. Canet, Localized diffusion measurements with a single B_1 gradient, in "Proceedings, 2nd International Conference on Magnetic Resonance Microscopy," p. 68, Heidelberg (1993).
26. E. Mischler, F. Humbert, B. Diter, and D. Canet, Measurement of one-dimensional spatially resolved self-diffusion coefficients and longitudinal relaxation times with a single B_1 gradient, *J. Magn. Reson. B* **106,** 32 (1995).
27. F. Humbert, E. Mischler, and D. Canet, Mesures globale et localisée du coefficient d'autodiffusion par gradients de champ radiofréquence, *J. Chim. Phys.* **92,** 1905 (1995).
28. R. Kimmich, B. Simon, and H. Köstler, Magnetization-grid rotating-frame imaging technique for diffusion and flow measurements, *J. Magn. Reson. A* **112,** 7 (1995).
29. B. Simon, R. Kimmich, and H. Köstler, Rotating-frame-imaging technique for spatially resolved diffusion and flow studies in the fringe field of RF probe coils, *J. Magn. Reson. A* **118,** 78 (1996).
30. F. Humbert, M. Valtier, A. Retournard, and D. Canet, Diffusion measurements using radio-frequency field gradient: Artifacts, remedies , practical hints, *J. Magn. Reson.* **134,** 245 (1998).
31. D. Canet, Radiofrequency field gradient experiments, *Progr NMR Spectrosc.* **30,** 101 (1997).
32. P. Maffei, P. Mutzenhardt, A. Retournard, B. Diter, R. Raulet, J. Brondeau, and D. Canet, NMR microscopy by radiofrequency field gradients, *J. Magn. Reson. A* **107,** 40 (1994).
33. P. T. Callaghan, "Priniples of Nuclear Magnetic Resonance Microscopy," Oxford Univ. Press, Oxford (1993).

34. F. Humbert, B. Diter, and D. Canet, NMR Microscopy by strong radiofrequency-field gradients with spaial resolution better than five micrometers, *J. Magn. Reson. A* **123,** 242 (1996).

35. Yi-Qiao Song, Boyd M. Goodson, B. Sheridan, T. M. de Swiet, and A. Pines, Effects of diffusion on magnetic resonance imaging of laser-polarized xenon gas, *J. Chem. Phys.* **108,** 6233 (1998).

36. P. P. Mitra and P. N. Sen, Effects of microgeometry and surface relaxation on NMR pulsed-field-gradient experiments: Simple pore geometries, *Phys. Rev. B* **41,** 143 (1992).

37. E. O. Stejskal and J. Tanner, Spin diffusion measurements: Spin echoes in the presence of a time-dependent field gradient, *J. Chem. Phys.* **42,** 288 (1965).

38. B. Pütz, D. Barsky, and K. Schulten, Edge enhancement by diffusion in microscopic magnetic resonance imaging, *J. Magn. Reson.* **97,** 27 (1992).

39. P. T. Callaghan, A. Coy, L. C. Forde, and C. J. Rofe, Diffusive relaxation and edge enhancement in NMR microscopy, *J. Magn. Reson. A* **101,** 347 (1993).

40. L. A. Weisenberger and J. L. Koenig, NMR Imaging of diffusion processes in polymers: Measurement of the spatial dependence of solvent mobility in partially swollen PMMA rods, *Macromolecules* **23,** 2445 (1990).

41. M. R. Krejsa and J. L. Koenig, NMR imaging studies of vulcanized butyl rubber, *Rubber Chem. Technol.* **64,** 635 (1991).

42. D. Le Bihan, Molecular diffusion, tissue microdynamics and microstructure, *NMR Biomed.* **8,** 375 (1995).